

Implementing a Universal Gate Set on a Logical Qubit Encoded in an Oscillator

Reinier W. Heeres,^{1,*} Philip Reinhold,^{1,*} Nissim Ofek,¹ Luigi Frunzio,¹ Liang Jiang,¹ Michel H. Devoret,¹ and Robert J. Schoelkopf¹

¹*Departments of Physics and Applied Physics, Yale University, New Haven, Connecticut 06520, USA*

A logical qubit is a two-dimensional subspace of a higher dimensional system, chosen such that it is possible to detect and correct the occurrence of certain errors [1]. Manipulation of the encoded information generally requires arbitrary and precise control over the entire system [2, 3]. Whether based on multiple physical qubits or larger dimensional modes such as oscillators, the individual elements in realistic devices will always have residual interactions which must be accounted for when designing logical operations. Here we demonstrate a holistic control strategy which exploits accurate knowledge of the Hamiltonian to manipulate a coupled oscillator-transmon system. We use this approach to realize high-fidelity (99%, inferred), decoherence-limited operations on a logical qubit encoded in a superconducting cavity resonator using four-component cat states [4, 5]. Our results show the power of applying numerical techniques [6] to control linear oscillators and pave the way for utilizing their large Hilbert space as a resource in quantum information processing.

Quantum error correction (QEC) aims at the creation of logical qubits whose information storage and processing capabilities exceed those of its constituent parts. Significant progress has been made toward quantum state preservation by repeated error detection using stabilizer measurements in trapped ions [3, 7], nitrogen vacancy centers [8], and superconducting circuits [9–11]. In order to go beyond storage and to manipulate the encoded information, one must perform operations on the whole system in such a way that it results in the desired transformation within the two-dimensional subspace defining the logical qubit. Any encoding scheme will consist of multiple interacting components where the system dynamics are not naturally confined within the logical subspace. Therefore, implementing operations requires carefully tailored controls which address each component of the system and manage their mutual interactions. Recent efforts have achieved this level of control and have demonstrated operations on a 5 qubit code in nuclear spin ensembles [2] and a 7 qubit code in trapped ions [3].

An alternative to logical qubit implementations based on multiple two level systems is to encode quantum information in continuous variable systems or oscillators, for which

there are several schemes [12, 13]. In particular so called “cat states”, which are superpositions of coherent states, can be used as the logical states of an encoded qubit [4]. They are attractive because coherent states are eigenstates of the photon annihilation operator (\hat{a}) and therefore single-photon loss induces simple, tractable errors.

Replacing several two level systems by an oscillator drastically reduces the hardware cost and complexity by requiring fewer components to fabricate and manipulate. However, introducing higher dimensional modes raises the issue of how to realize complete control over the system. Driving an isolated harmonic oscillator results in a displacement operation, which can only produce coherent states from the vacuum. Any oscillator-based logical qubit scheme will require a richer class of operations, which one can access via coupling to a nonlinear system. In the case of a frequency-tunable qubit coupled to an oscillator with the Jaynes-Cummings (JC) interaction ($H_{JC} = \sigma_+ \hat{a} + \sigma_- \hat{a}^\dagger$), it has been demonstrated that it is possible to prepare arbitrary states in the oscillator [14, 15].

In the far off-resonant case, where the JC interaction reduces to the dispersive Hamiltonian ($H_d/\hbar = \chi \hat{a}^\dagger a |e\rangle\langle e|$), a small set of operations acting on a timescale of $2\pi/\chi$ is in principle sufficient for universal control [16, 17] and has been used for non-trivial operations [18, 19]. Generally, however, any approach decomposing an arbitrary operation into a sequence of elementary gates generates only a small subset of physically allowed control fields. It therefore suffers from two issues limiting the achievable fidelity. First, the constructed sequences may require an unacceptably large number of gates, limiting operations which are feasible in the presence of decoherence. Second, the idealized model used by a constructive approach typically fails to account for the existence of higher order Hamiltonian terms such as the Kerr non-linearity $H_{\text{Kerr}}/\hbar = \frac{\kappa}{2} (\hat{a}^\dagger)^2 \hat{a}^2$ and spurious residual couplings in multi-qubit systems.

In this work we address these problems by considering a full model of the time dependent Hamiltonian in the presence of arbitrary control fields. Nuclear magnetic resonance experiments have shown that, if the available controls are universal, numerical optimization procedures can reliably solve the inversion problem of finding control fields to implement an intended operation. These optimal control algorithms, in particular the Gradient Ascent Pulse Engineering (GRAPE) method [6, 20], have been successfully employed in a variety of other fields [21, 22]. Since GRAPE crucially depends on the

* reinier@heeres.eu; These authors contributed equally

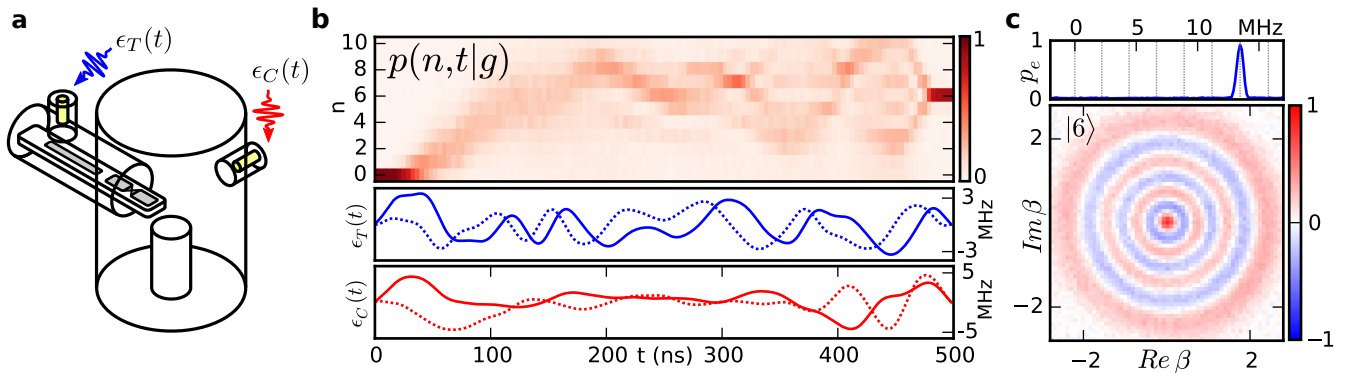


FIG. 1. **Experimental system and demonstration of control strategy.** **a**, Schematic drawing of the experimental system. A $\lambda/4$ coax-stub cavity resonator is coupled to a transmon and readout resonator on a sapphire substrate. Input couplers close to the transmon and cavity deliver the respective time-dependent microwave control fields $\epsilon_T(t)$ and $\epsilon_C(t)$. **b**, Lower panel: optimized transmon and oscillator control waveforms of length approximately $2\pi/\chi$ to take the oscillator from vacuum to the 6-photon Fock state. Solid (dotted) lines represent the in-phase (quadrature) field component. Upper panel: oscillator photon-number population trajectory versus time conditioned on transmon in $|g\rangle$. A complex trajectory occupying a wide range of photon numbers is taken to perform the intended operation. **c**, Characterization of the oscillator state using Wigner tomography (bottom) and transmon spectroscopy (top), where grey dashed lines indicate the transition frequency associated with the first 7 Fock states. The single peak in the spectroscopy data directly reveals the oscillator's population due to the dispersive interaction giving a frequency shift of $6\chi/2\pi \approx 13$ MHz.

model of the system, its successful application is powerful evidence that the Hamiltonian used accurately captures the system dynamics over a broad range of driving conditions.

The physical system used in our experiments is schematically depicted in Fig. 1a. The seamless aluminum $\lambda/4$ coax-stub cavity resonator [23] with a fundamental frequency 4452.6 MHz has an energy relaxation time of 2.7 ms. A single-junction transmon with transition frequency 5664.0 MHz and anharmonicity of 236 MHz is dispersively coupled to the oscillator, resulting in an interaction term $\chi \hat{a}^\dagger \hat{a} |e\rangle \langle e|$, with $\chi/2\pi = -2.2$ MHz. Crucially, additional higher order terms are determined accurately through a separate set of calibration experiments (Table SI, Supplementary Information). Control of the system is implemented through full in-phase/quadrature (IQ) modulated microwave fields centered on the transmon (oscillator) frequency and sent to the pin coupling to the transmon (oscillator) mode. In the rotating wave approximation, this results in the drive Hamiltonian $H_c/\hbar = \epsilon_C a + \epsilon_T \sigma_- + \text{h.c.}$ Modulation using an arbitrary waveform generator allows the coefficients ϵ_C and ϵ_T to be arbitrary complex-valued functions of time.

As an example application of GRAPE to our system, we find $\epsilon_C(t)$ and $\epsilon_T(t)$ such that, starting from the vacuum, after 500 ns of driven evolution the system ends up in the state $|g, 6\rangle$ (Fig. 1bc). This highly nontrivial operation, effectively realizing a $|6\rangle\langle 0|$ coupling term on the oscillator, is enabled by the dispersive Hamiltonian using only linear drives on the transmon and the oscillator.

Using this control strategy, we can target the creation and manipulation of a logical qubit encoded in an even-parity four-component cat subspace. Omitting normalization, the

code states in this subspace can be written as

$$|\pm Z_L\rangle = |\alpha\rangle + |-\alpha\rangle \pm |i\alpha\rangle \pm |-i\alpha\rangle \quad (1)$$

where we use $\alpha = \sqrt{3}$. These code words are both of even photon number parity, and are distinguished by their photon number modulo 4:

$$|+Z_L\rangle = \sum_n \frac{\alpha^{4n}}{\sqrt{(4n)!}} |4n\rangle \quad (2)$$

$$|-Z_L\rangle = \sum_n \frac{\alpha^{4n+2}}{\sqrt{(4n+2)!}} |4n+2\rangle \quad (3)$$

Single photon loss, the dominant error channel for the system, transforms both code words to states of odd photon number parity. The encoded information, however, is preserved by this process as long as one can keep track of the number of photons that have been lost. Since parity measurements can be performed efficiently and non-destructively [24], single photon loss is a correctable error [5].

Using GRAPE, we create a universal set of gates on our logical qubit, which includes X and Y rotations by π and $\pi/2$, as well as Hadamard and T gates. These pulses are each 1100 ns $\approx 2.4 \times 2\pi/\chi$ in length with a 2 ns time resolution, although 99% of the spectral content lies within a bandwidth of 33 MHz (27 MHz) for the transmon (oscillator) drive (Fig. S2, Supplementary Information). Each operation is designed to begin and end with the transmon in the ground state. Additionally, we create encode (U_{enc}) and decode (U_{dec}) pulses to transfer a bit of quantum information between our transmon $\{|g, 0\rangle, |e, 0\rangle\}$ subspace, which we

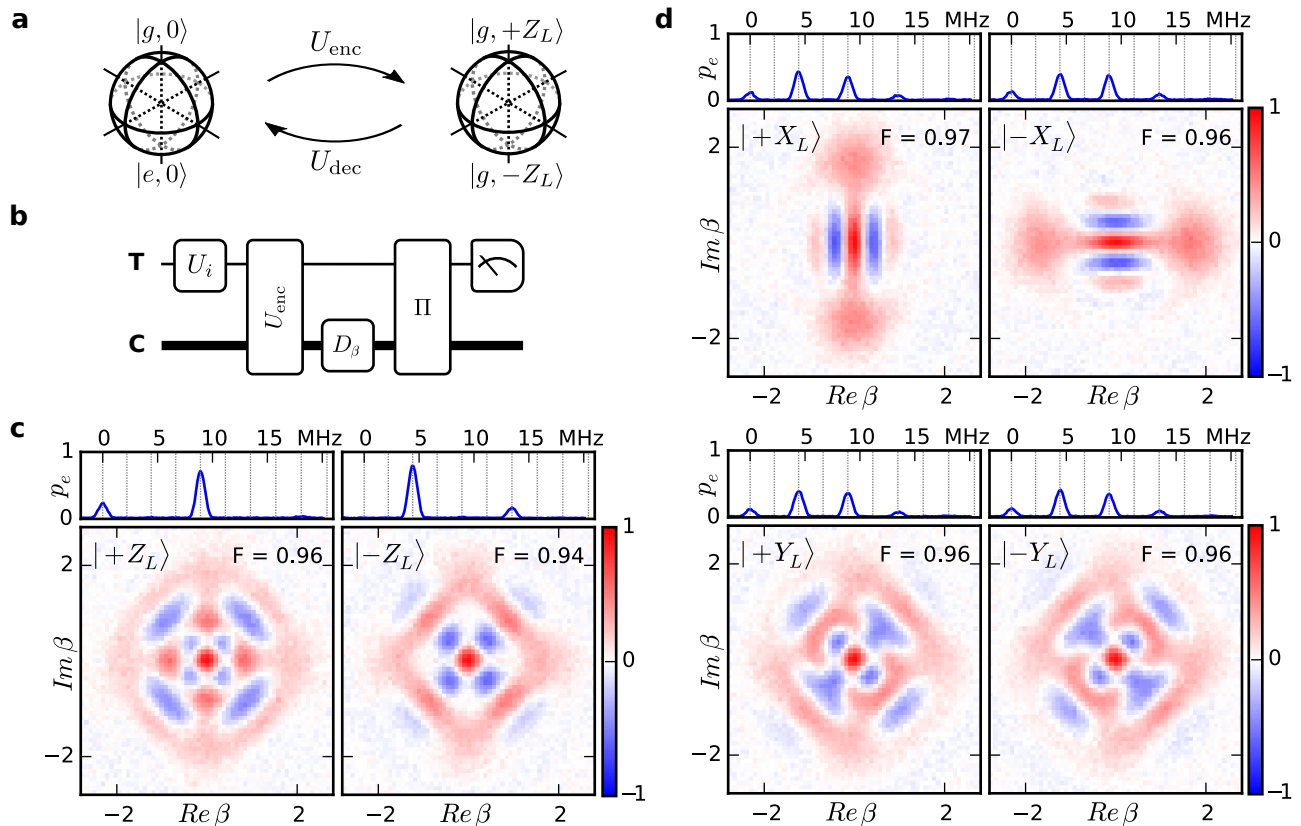


FIG. 2. **Characterization of encoded states.** **a**, U_{enc} and U_{dec} are operations which coherently map between two distinct two-dimensional subspaces, represented by Bloch spheres. The first subspace consists of the transmon $|g\rangle$ and $|e\rangle$ levels, with the oscillator in the vacuum. The second is given by the oscillator-encoded states $|+Z_L\rangle$ and $|-Z_L\rangle$ (Eq. 1), with the transmon in the ground state. **b**, Wigner tomography sequence which characterizes the encoded states. A transmon state is prepared by applying an initial rotation U_i and is mapped to the oscillator using U_{enc} . An oscillator displacement D_β followed by a parity mapping operation Π (implemented using an optimal control pulse) allows one to measure the oscillator Wigner function $W(\beta)$. The transmon can be re-used to measure the oscillator's parity because the encoding pulse leaves the transmon in the ground state with high probability ($p > 98\%$). **c**, Applying U_{enc} to the transmon states $|g\rangle$ and $|e\rangle$ produces states whose Wigner functions are consistent with the intended encoded basis states (Eq. 1). A transmon spectroscopy experiment (top panel) illustrates that only photon number states with $n = 0 \bmod 4$ and $n = 2 \bmod 4$ are present for logical state $|+Z_L\rangle$ and $|-Z_L\rangle$ respectively. **d**, Applying U_{enc} to superpositions of the transmon basis states demonstrates that the relative phase is preserved and that U_{enc} is a faithful map between the transmon and logical qubit Bloch spheres. These states, on the equator of the Bloch sphere, are equally weighted superpositions of $|+Z_L\rangle$ and $|-Z_L\rangle$ and therefore contain all even photon numbers present in the basis states.

can easily prepare and measure, and our encoded subspace $\{|g, +Z_L\rangle, |g, -Z_L\rangle\}$ (Fig. 2a).

We characterize the encode operation by preparing all 6 cardinal points on the transmon Bloch sphere, applying the encode pulse and performing Wigner tomography on the oscillator (Fig. 2b–d). Maximum likelihood reconstruction of the density matrix associated with the measured Wigner functions indicates an average fidelity of 0.96. This metric underestimates the fidelity of U_{enc} because it is affected by several sources of error not intrinsic to the encoding operation itself, including error in the parity mapping and measurement infidelity.

Process tomography provides a full characterization of a

quantum operation, but depends on pre-existing trusted operations and measurements which are not available for our encoded subspace. However, an indirect characterization of a gate U_X on our logical qubit can be performed using the operation $U_{\text{dec}}U_XU_{\text{enc}}$, which maps the transmon subspace onto itself. This allows one to use the trusted state preparations and measurements on the transmon to perform tomography on the composite process (Fig. 3a). The reconstructed process matrices show qualitative agreement with the intended encoded qubit gates. We can break the calculated infidelity down into 3 parts: transmon preparation and measurement error, encode-decode error and gate error. Using the experimentally determined process fidelities both without any op-

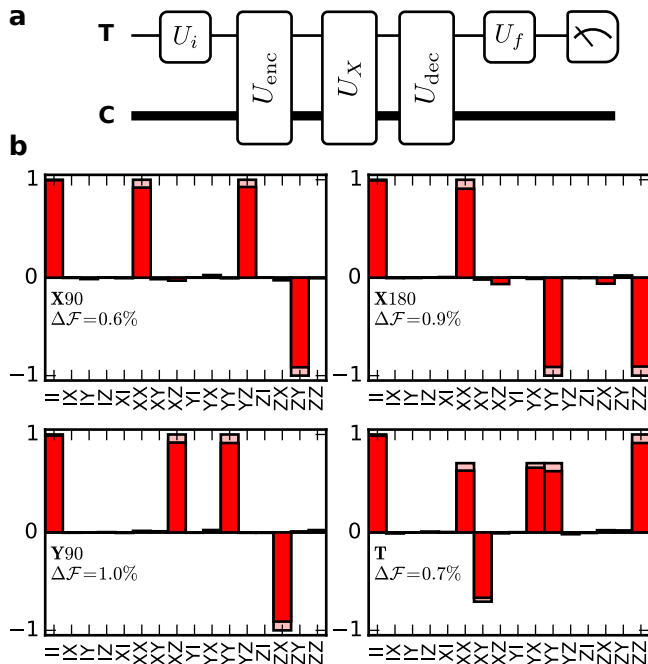


FIG. 3. **Process tomography of operations on encoded qubit.** **a**, In order to characterize a gate U_X on the encoded qubit, transmon process tomography is performed on the operation $U_{\text{dec}}U_XU_{\text{enc}}$. Process tomography is implemented by performing an initial transmon rotation U_i right after state preparation, as well as a final transmon rotation U_f , right before measurement of the transmon. **b**, Process tomography results for selected operations (for additional operations, see Fig. S7, Supplementary Information). The process tomography yields an estimated quantum channel G . We represent this channel in the Pauli transfer representation. The bar labeled with operators AB represents $\text{Tr}(AG(B))/2$. Red and pink bars indicate the experimental and ideal values, respectively. The infidelity $\Delta\mathcal{F}_{\text{PT}}$ of operation U_X is estimated as the difference between $\mathcal{F}_{\text{PT}}(U_{\text{dec}}U_XU_{\text{enc}})$ and $\mathcal{F}_{\text{PT}}(U_{\text{dec}}U_{\text{enc}}) = 0.964$. The selected set of operations, $\{X180, X90, Y90, T\}$, allows universal control of the logical qubit.

eration $\mathcal{F}_{\text{PT}}(\text{No Op.}) = 0.982$, as well as with the encode and decode pulses $\mathcal{F}_{\text{PT}}(U_{\text{dec}}U_{\text{enc}}) = 0.964$, we estimate an infidelity contribution of approximately 1.8% for each of the first two components. To account for these factors to first order, the infidelity of operations on the encoded qubit are reported relative to $\mathcal{F}_{\text{PT}}(U_{\text{dec}}U_{\text{enc}})$. We find an average infidelity of 0.75% over our set of 9 gates (Table I).

In order to establish the fidelity of this set of operations more accurately, we perform randomized benchmarking [25] (RB) on our encoded qubit (Fig. 4a). From the resulting data (Fig. 4c) we infer an average gate fidelity of 0.991. The infidelity of each of the individual gates is isolated using interleaved randomized benchmarking [26] (iRB), which alternates between a single fixed and a random gate (Fig. 4b). Comparing the fitted decay constants of the RB and iRB re-

Gate	$1 - \mathcal{F}_{\text{RB}}$ (%)	$\Delta\mathcal{F}_{\text{PT}}$ (%)	$1 - \mathcal{F}_{\text{sim}}$ (%)
I	0.46 ± 0.02	0.51	0.31
X90	0.79 ± 0.02	0.57	0.78
-X90	0.91 ± 0.03	0.71	0.83
X180	1.11 ± 0.03	0.88	1.09
Y90	0.96 ± 0.03	0.98	0.76
-Y90	0.81 ± 0.02	0.52	0.75
Y180	1.28 ± 0.03	0.99	1.67
H	0.93 ± 0.03	0.86	1.00
average	0.90 ± 0.02	0.75	0.90
$U_{\text{enc}}U_{\text{dec}}$	1.70 ± 0.03	1.39	1.76
T	-	0.71	0.40

TABLE I. **Operation fidelities.** Measured and simulated gate infidelities. All fidelities reported are average gate fidelities $\mathcal{F}(\mathcal{E}_1, \mathcal{E}_2) \equiv \int d\psi F(\mathcal{E}_1(\psi), \mathcal{E}_2(\psi))$, where F is the usual quantum state fidelity $F(\rho_1, \rho_2) = \text{Tr}(\sqrt{\rho_1\rho_2}\sqrt{\rho_1})$. \mathcal{F}_{RB} , $\Delta\mathcal{F}_{\text{PT}}$ and \mathcal{F}_{sim} are the values extracted from interleaved randomized benchmarking, process tomography (see Fig. 3) and simulations using the Lindblad master equation respectively. The row labeled “average” gives the fidelities averaged over the first 8 gates, which is the set used in the standard randomized benchmarking experiment.

sults allows us to extract the fidelity of the fixed gate. The results are summarized in Table I, together with the gate fidelities based on process tomography (Fig. 3) and Lindblad master equation simulations accounting for finite T_1 and T_2 of the transmon and oscillator (see Supplementary Information). We note that all gates are implemented with an approximately equal infidelity of 1% and that process tomography and iRB yield consistent results. While several sources of decoherence are accounted for in the master equation simulations, the dominant source of infidelity in the model is transmon dephasing ($T_2 \approx 43 \mu\text{s}$). The strong agreement between simulations and experiment indicates that the infidelity is primarily caused by decoherence and that additional contributions associated with imperfections in the model Hamiltonian and the applied pulses are a significantly smaller effect.

In conclusion, we have demonstrated a high-fidelity implementation of a universal set of gates on a qubit encoded into an oscillator using the cat-code. The low error rates for these operations are verified using both process tomography and randomized benchmarking, and the results are consistent with simulations which account for decoherence. We obtained these operations by numerically optimizing time-dependent drives which make use of the well-characterized dispersive interaction between the far detuned oscillator and transmon modes. While in this Letter we have focused on realizing and characterizing single-qubit operations on cat-encoded qubits, this control technique is not restricted to these goals, and is in principle capable of crafting arbitrary unitary operations on the transmon-oscillator system. The high quality of these operations depends critically on

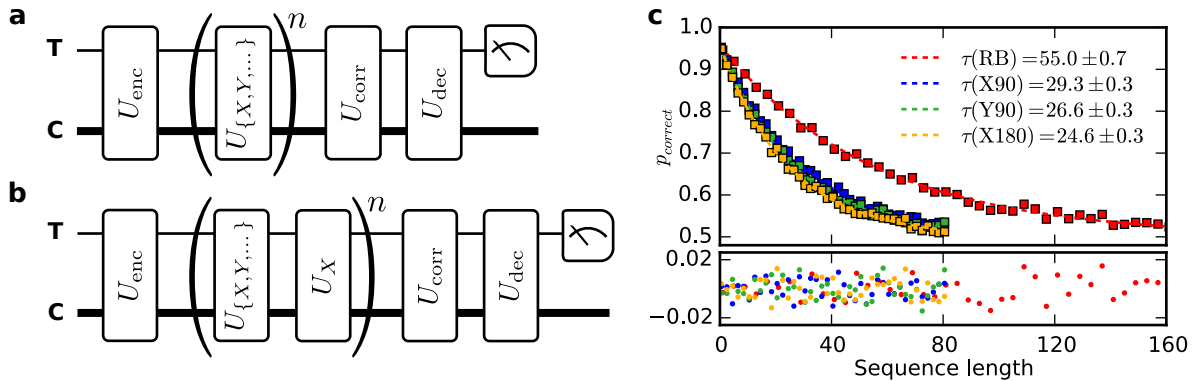


FIG. 4. **Randomized benchmarking of operations on encoded qubit.** **a**, Randomized benchmarking (RB) sequence. In RB a sequence of Clifford operations of length n is chosen at random ($U_{\{X,Y,\dots\}}$), followed by the operation which inverts the effect of the sequence (U_{corr}). In order to apply this technique to the operations on the encoded qubit, we begin the experiment by encoding, and decode before measurement. Our implementation of RB creates a new random gate sequence for every measurement, and is thus not biased by the distribution of sequences which are measured. **b**, Interleaved randomized benchmarking (iRB) sequence: In order to establish the fidelity of a single operation (here, U_X), the operation is interleaved with random operations, and the benchmarking result is compared with the non-interleaved case. **c**, The probability of measuring the correct result versus sequence length n is fit to a two parameter model $p_{\text{correct}} = 0.5 + Ae^{-n/\tau}$. The lower panel shows the fit residuals. Each data point is the result of 2000 averages, with a new sequence realization every shot. The error averaged over all gates is computed as $r = (1 - e^{-1/\tau(\text{RB})})/2$ [25]. The average error for a single gate X is computed as $r(X) = (1 - e^{1/\tau(X) - 1/\tau(\text{RB})})/2$ [26].

an accurate characterization of the system Hamiltonian, and demonstrates the utility of numerical optimal control for realizing quantum information processing.

I. ACKNOWLEDGMENTS

We would like to thank Katrina Sliwa and Michael Hatridge for providing the parametric amplifier, Chris Axline, Jacob Blumoff, Kevin Chou and Chen Wang for discussions

regarding sample design, Stefan Krastanov, Chao Shen and Victor Albert for discussions on universal control and Steve Flammia and Robin Blume-Kohout for advice about tomography. This research was supported by the U.S. Army Research Office (W911NF-14-1-011). P.R. was supported by the U.S. Air Force Office of Scientific Research (FA9550-15-1-0015), L.J. by the Alfred P. Sloan Foundation and the Packard Foundation. Facilities use was supported by the Yale Institute for Nanoscience and Quantum Engineering (YINQE), the Yale SEAS cleanroom, and the National Science Foundation (MRSECDMR-1119826).

-
- [1] Barbara M Terhal. Quantum error correction for quantum memories. *Rev. Mod. Phys.*, 87(2):307–346, April 2015.
 - [2] Jingfu Zhang, Raymond Laflamme, and Dieter Suter. Experimental Implementation of Encoded Logical Qubit Operations in a Perfect Quantum Error Correcting Code. *Phys. Rev. Lett.*, 109(10):100503, September 2012.
 - [3] D Nigg, M Müller, E A Martinez, P Schindler, M Henrich, T Monz, M A Martin-Delgado, and R Blatt. Quantum computations on a topologically encoded qubit. *Science*, 345(6194):302–305, July 2014.
 - [4] Mazyar Mirrahimi, Zaki Leghtas, Victor V Albert, Steven Touzard, Robert J Schoelkopf, Liang Jiang, and Michel H Devoret. Dynamically protected cat-qubits: a new paradigm for universal quantum computation. *New J. Phys.*, 16(4), 2014.
 - [5] Nissim Ofek, Andrei Petrenko, Reinier Heeres, Philip Reinhold, Zaki Leghtas, Brian Vlastakis, Yehan Liu, Luigi Frunzio, SM Girvin, Liang Jiang, M Mirrahimi, M H Devoret, and R J Schoelkopf. Extending the lifetime of a quantum bit with error correction in superconducting circuits. *Nature*, advance online publication, Jul 2016.
 - [6] Navin Khaneja, Timo Reiss, Cindie Kehlet, Thomas Schulte-Herbrüggen, and Steffen J Glaser. Optimal control of coupled spin dynamics: design of NMR pulse sequences by gradient ascent algorithms. *J. Mag. Res.*, 172(2):296–305, February 2005.
 - [7] J Chiaverini, D Leibfried, T Schaetz, MD Barrett, RB Blakestad, J Britton, WM Itano, JD Jost, E Knill, C Langer, et al. Realization of quantum error correction. *Nature*, 432(7017):602–605, 2004.
 - [8] J Cramer, N Kalb, M A Rol, B Hensen, M S Blok, M Markham, D J Twitchen, R Hanson, and T H Taminau. Repeated quantum error correction on a continuously en-

- coded qubit by real-time feedback. *Nature Communications*, 7:11526, May 2016.
- [9] J Kelly, R Barends, Austin G Fowler, A Megrant, E Jeffrey, T C White, D Sank, J Y Mutus, B Campbell, Yu Chen, Z Chen, B Chiaro, A Dunsworth, I C Hoi, C Neill, P J J O'Malley, C Quintana, P Roushan, A Vainsencher, J Wenner, Andrew N Cleland, and John M Martinis. State preservation by repetitive error detection in a superconducting quantum circuit. *Nature*, 519(7541):66–69, March 2015.
- [10] D Ristè, S Poletto, M Z Huang, A Bruno, V Vesterinen, O P Saira, and L DiCarlo. Detecting bit-flip errors in a logical qubit using stabilizer measurements. *Nature Communications*, 6:6983, April 2015.
- [11] A D Córcoles, Easwar Magesan, Srikanth J Srinivasan, Andrew W Cross, M Steffen, Jay M Gambetta, and Jerry M Chow. Demonstration of a quantum error detection code using a square lattice of four superconducting qubits. *Nature Communications*, 6:6979, April 2015.
- [12] Daniel Gottesman, Alexei Kitaev, and John Preskill. Encoding a qubit in an oscillator. *Phys. Rev. A*, 64(1):012310, June 2001.
- [13] Marios H Michael, Matti Silveri, R T Brierley, Victor V Albert, Juha Salmilehto, Liang Jiang, and Steven M Girvin. New Class of Quantum Error-Correcting Codes for a Bosonic Mode. *Phys. Rev. X*, 6(3):031006, July 2016.
- [14] C K Law and J H Eberly. Arbitrary Control of a Quantum Electromagnetic Field. *Phys. Rev. Lett.*, 76(7):1055–1058, February 1996.
- [15] Max Hofheinz, H Wang, M Ansmann, Radoslaw C Bialczak, Erik Lucero, M Neeley, A D O'Connell, D Sank, J Wenner, John M Martinis, and Andrew N Cleland. Synthesizing arbitrary quantum states in a superconducting resonator. *Nature*, 459(7246):546–549, 2009.
- [16] Stefan Krastanov, Victor V Albert, Chao Shen, Chang-Ling Zou, Reinier W Heeres, Brian Vlastakis, Robert J Schoelkopf, and Liang Jiang. Universal control of an oscillator with dispersive coupling to a qubit. *Phys. Rev. A*, 92(4):040303, October 2015.
- [17] Simon E Nigg. Deterministic Hadamard gate for microwave cat-state qubits in circuit QED. *Phys. Rev. A*, 89(2):022340, February 2014.
- [18] Brian Vlastakis, Gerhard Kirchmair, Zaki Leghtas, Simon E Nigg, Luigi Frunzio, Steven M Girvin, Mazyar Mirrahimi, Michel H Devoret, and Robert J Schoelkopf. Deterministically Encoding Quantum Information Using 100-Photon Schrödinger Cat States. *Science*, 342(6158):607–610, November 2013.
- [19] Reinier W Heeres, Brian Vlastakis, Eric Holland, Stefan Krastanov, Victor V Albert, Luigi Frunzio, Liang Jiang, and Robert J Schoelkopf. Cavity State Manipulation Using Photon-Number Selective Phase Gates. *Phys. Rev. Lett.*, 115(13):137002, September 2015.
- [20] P de Fouquieres, SG Schirmer, SJ Glaser, and Ilya Kuprov. Second order gradient ascent pulse engineering. *J. Mag. Res.*, 212(2):412–417, 2011.
- [21] Florian Dolde, Ville Bergholm, Ya Wang, Ingmar Jakobi, Boris Naydenov, Sébastien Pezzagna, Jan Meijer, Fedor Jelezko, Philipp Neumann, Thomas Schulte-Herbrüggen, Jacob Biamonte, and Jörg Wrachtrup. High-fidelity spin entanglement using optimal control. *Nature Communications*, 5, February 2014.
- [22] B E Anderson, H Sosa-Martinez, C A Riofrío, Ivan H Deutsch, and Poul S Jessen. Accurate and Robust Unitary Transformations of a High-Dimensional Quantum System. *Phys. Rev. Lett.*, 114(24):240401, June 2015.
- [23] Matthew Reagor, Wolfgang Pfaff, Christopher Axline, Reinier W. Heeres, Nissim Ofek, Katrina Sliwa, Eric Holland, Chen Wang, Jacob Blumoff, Kevin Chou, Michael J. Hatridge, Luigi Frunzio, Michel H. Devoret, Liang Jiang, and Robert J. Schoelkopf. Quantum memory with millisecond coherence in circuit qed. *Phys. Rev. B*, 94:014506, Jul 2016.
- [24] L Sun, A Petrenko, Z Leghtas, B Vlastakis, G Kirchmair, KM Sliwa, A Narla, M Hatridge, S Shankar, J Blumoff, L Frunzio, M Mirrahimi, Devoret M H, and R J Schoelkopf. Tracking photon jumps with repeated quantum non-demolition parity measurements. *Nature*, 511:444–448, 2014.
- [25] Easwar Magesan, Jay M Gambetta, and Joseph Emerson. Scalable and Robust Randomized Benchmarking of Quantum Processes. *Phys. Rev. Lett.*, 106(18):180504, May 2011.
- [26] Easwar Magesan, Jay M Gambetta, Blake R Johnson, Colm A Ryan, Jerry M Chow, Seth T Merkel, Marcus P da Silva, George A Keefe, Mary B Rothwell, Thomas A Ohki, Mark B Ketchen, and M Steffen. Efficient Measurement of Quantum Gate Error by Interleaved Randomized Benchmarking. *Phys. Rev. Lett.*, 109(8):080505, August 2012.
- [27] Richard H Byrd, Peihuang Lu, Jorge Nocedal, and Ciyong Zhu. A limited memory algorithm for bound constrained optimization. *SIAM Journal on Scientific Computing*, 16(5):1190–1208, 1995.
- [28] I Najfeld and T F Havel. Derivatives of the Matrix Exponential and Their Computation. *Advances in Applied Mathematics*, 16(3):321–375, September 1995.
- [29] F Motzoi, Jay M Gambetta, S T Merkel, and F K Wilhelm. Optimal control methods for rapidly time-varying Hamiltonians. *Phys. Rev. A*, 84(2):022307, August 2011.
- [30] D J Egger and F K Wilhelm. Adaptive Hybrid Optimal Quantum Control for Imprecisely Characterized Systems. *Phys. Rev. Lett.*, 112(24):240503, June 2014.
- [31] J Kelly, R Barends, B Campbell, Y Chen, Z Chen, B Chiaro, A Dunsworth, Austin G Fowler, I C Hoi, E Jeffrey, A Megrant, J Mutus, C Neill, P J J O'Malley, C Quintana, P Roushan, D Sank, A Vainsencher, J Wenner, T C White, Andrew N Cleland, and John M Martinis. Optimal Quantum Control Using Randomized Benchmarking. *Phys. Rev. Lett.*, 112(24):240504, June 2014.
- [32] Gerhard Kirchmair, Brian Vlastakis, Zaki Leghtas, Simon E Nigg, Hanhee Paik, Eran Ginossar, Mazyar Mirrahimi, Luigi Frunzio, Steven M Girvin, and Robert J Schoelkopf. Observation of quantum state collapse and revival due to the single-photon kerr effect. *Nature*, 495(7440):205–209, 2013.

System Parameter	Hamiltonian Term	Parameter Value
Transmon frequency	$\omega_T \hat{b}^\dagger \hat{b}$	$2\pi \times 5664.0$ MHz
Oscillator frequency	$\omega_C \hat{a}^\dagger \hat{a}$	$2\pi \times 4452.6$ MHz
Dispersive shift	$\chi \hat{a}^\dagger \hat{a} \hat{b}^\dagger \hat{b}$	$2\pi \times -2194 \pm 3$ kHz
Transmon anharmonicity	$\frac{\alpha}{2} (\hat{b}^\dagger)^2 \hat{b}^2$	$2\pi \times -236$ MHz
Oscillator anharmonicity (Kerr)	$\frac{K}{2} (\hat{a}^\dagger)^2 \hat{a}^2$	$2\pi \times -3.7 \pm 0.1$ kHz
Second order dispersive shift	$\frac{\chi'}{2} (\hat{a}^\dagger)^2 \hat{a}^2 \hat{b}^\dagger \hat{b}$	$2\pi \times -19.0 \pm 0.4$ kHz
Transmon relaxation	$\frac{1}{T_1} D[\hat{b}]$	$170 \pm 10 \mu s$
Transmon dephasing	$\frac{1}{T_\phi} D[\hat{b}^\dagger \hat{b}]$	$43 \pm 5 \mu s$
Oscillator relaxation	$\frac{1}{T_{\text{cav}}} D[\hat{a}]$	$2.7 \pm 0.1 ms$

TABLE SI. **Measured system parameters** The dispersive shift and its second order correction are determined using transmon spectroscopy experiments (Fig. S1). The oscillator anharmonicity is determined by fitting a set of Wigner functions after different lengths of free evolution time.

Supplementary Material

I. SYSTEM HAMILTONIAN

Here we give the full system Hamiltonian to the precision with which we have characterized it. We denote the annihilation operator corresponding to the oscillator (transmon) mode with \hat{a} (\hat{b}). Breaking down the system Hamiltonian into components representing the individual modes, their interactions, as well as driving terms, we can write

$$H(t) = H_{\text{oscillator}} + H_{\text{transmon}} + H_{\text{interaction}} + H_{\text{drive}}(t) \quad (4)$$

$$H_{\text{oscillator}}/\hbar = \omega_C \hat{a}^\dagger \hat{a} + \frac{K}{2} (\hat{a}^\dagger)^2 \hat{a}^2 \quad (5)$$

$$H_{\text{transmon}}/\hbar = \omega_T \hat{b}^\dagger \hat{b} + \frac{\alpha}{2} (\hat{b}^\dagger)^2 \hat{b}^2 \quad (6)$$

$$H_{\text{interaction}}/\hbar = \chi \hat{a}^\dagger \hat{a} \hat{b}^\dagger \hat{b} + \frac{\chi'}{2} \hat{b}^\dagger \hat{b} (\hat{a}^\dagger)^2 \hat{a}^2 \quad (7)$$

$$H_{\text{drive}}(t)/\hbar = \epsilon_C(t) \hat{a} + \epsilon_T(t) \hat{b} + \text{h.c.} \quad (8)$$

When simulating how known decoherence sources should impact the fidelity of our operations, we use a Markovian Lindblad master equation of the form:

$$\frac{\partial}{\partial t} \rho(t) = \frac{-i}{\hbar} [H(t), \rho(t)] + \left(\frac{1}{T_{1,C}} D[\hat{a}] + \frac{1}{T_{1,T}} D[\hat{b}] + \frac{1}{T_\phi} D[\hat{b}^\dagger \hat{b}] \right) (\rho(t)) \quad (9)$$

$$D[a](\rho) = a\rho a^\dagger - \frac{1}{2} \{a^\dagger a, \rho\} \quad (10)$$

The measured values for each of these system parameters are shown in table SI.

II. GRAPE IMPLEMENTATION

We define operations on our system in terms of a set of simultaneous state transfers, i.e. the operation should, for each i , take the initial state $|\psi_{\text{init}}^{(i)}\rangle$ to the corresponding final state $|\psi_{\text{final}}^{(i)}\rangle$. In order to prepare a desired operation on the joint oscillator-transmon Hilbert space, we use GRAPE to maximize the (coherent) average fidelity of these state transfers over the controls $\epsilon(t) \equiv (\epsilon_C(t), \epsilon_T(t))$:

$$\underset{\epsilon(t)}{\text{maximize}} \mathcal{F}(\epsilon(t)) \quad (11)$$

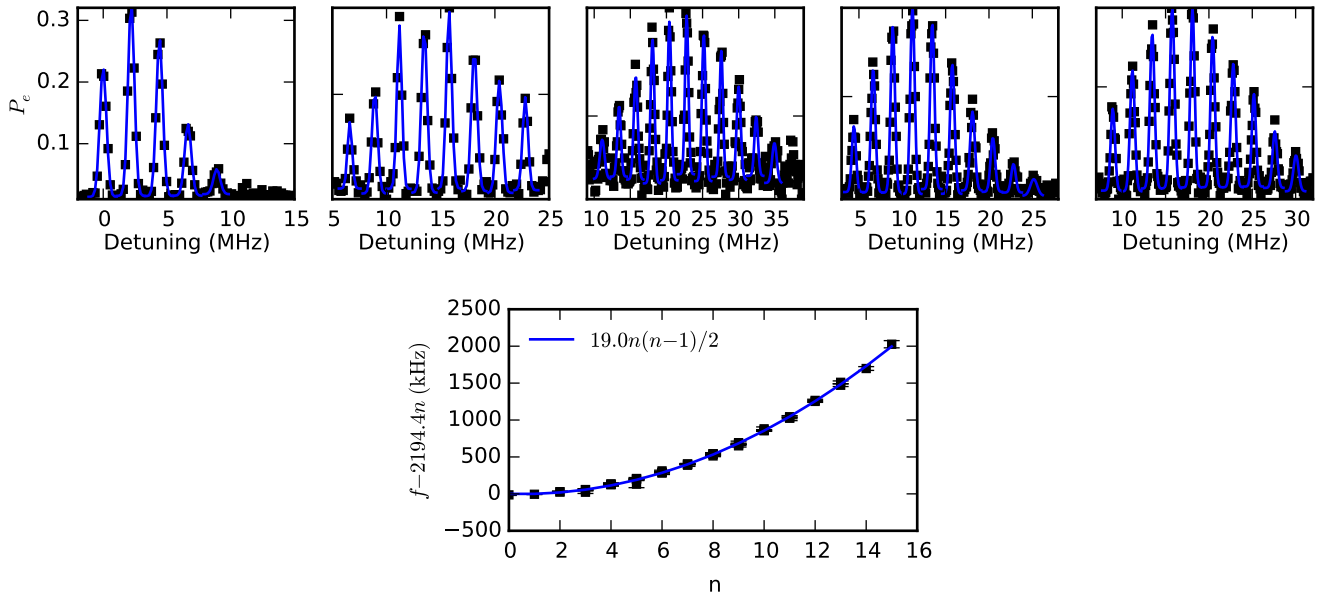


FIG. S1. **Dispersive shift measurement.** The dispersive shift χ and its second order correction term χ' are determined from transmon spectroscopy experiments with several different displacements (top). Each peak is fit to a Gaussian and the resulting center frequencies are fit using a quadratic model.

$$\mathcal{F}(\epsilon(t)) = \left| \sum_i \langle \psi_{\text{final}}^{(i)} | U(T, \epsilon(t)) | \psi_{\text{init}}^{(i)} \rangle \right|^2, \quad (12)$$

where the unitary U defined by the waveforms $\epsilon(t)$ is given by the time-ordered exponential of the Hamiltonian up to some final time T ,

$$U(T, \epsilon(t)) = \mathcal{T} \exp\left(-\int_0^T dt H(\epsilon(t))\right). \quad (13)$$

To make the problem numerically tractable, $\epsilon(t)$ is represented as a piecewise constant function with $N = T/\Delta t$ steps of length $\Delta t = 2$ ns, corresponding to the time resolution of our arbitrary waveform generator.

$$U(T, \epsilon(t)) = U_N U_{N-1} \cdots U_2 U_1 \quad (14)$$

$$U_k = \exp\left(\frac{i\Delta t}{\hbar} H(\epsilon(k\Delta t))\right) \quad (15)$$

Using 4 parameters per time point (real and imaginary components of the oscillator and transmon drives) and $N = 550$ time points representing the $1.1 \mu\text{s}$ pulse, there are 2200 parameters to optimize over. In order to carry out a numerical optimization with such a large number of parameters, it is crucial that one can efficiently calculate the gradient of the optimized function with respect to all of its parameters. In this case it is possible to use Quasi-Newton optimization algorithms, such as L-BFGS [27] in order to optimize the function with many fewer function evaluations. We can simplify the calculation of the gradient

as follows:

$$\frac{\partial \mathcal{F}}{\partial \epsilon_i(k\Delta t)} = 2 \left(\text{Re}(v) \text{Re} \left(\frac{\partial v}{\partial \epsilon_i(k\Delta t)} \right) + \text{Im}(v) \text{Im} \left(\frac{\partial v}{\partial \epsilon_i(k\Delta t)} \right) \right) \quad (16)$$

$$v \equiv \sum_i \langle \psi_{\text{final}}^{(i)} | U(T, \epsilon(t)) | \psi_{\text{init}}^{(i)} \rangle \quad (17)$$

$$\frac{\partial v}{\partial \epsilon_i(k\Delta t)} = \sum_i \langle \psi_{\text{final}}^{(i)} | \frac{\partial U(T, \epsilon(t))}{\partial \epsilon_i(k\Delta t)} | \psi_{\text{init}}^{(i)} \rangle \quad (18)$$

$$= \sum_i \langle \psi_{\text{final}}^{(i)} | U_N \cdots U_{k+1} \frac{\partial U_k}{\partial \epsilon_i(k\Delta t)} U_{k-1} \cdots U_1 | \psi_{\text{init}}^{(i)} \rangle \quad (19)$$

Therefore, the calculation of the gradient can be reduced to computing the states $U_{k-1} \cdots U_1 | \psi_{\text{init}}^{(i)} \rangle$, $U_{k+1}^\dagger \cdots U_N^\dagger | \psi_{\text{final}}^{(i)} \rangle$ as well as the gradient of the step propagator $\frac{\partial U_k}{\partial \epsilon_i(k\Delta t)}$. The states can be stored from the evaluation of the fidelity itself, and there are several efficient ways of evaluating the gradient of the propagator [28].

The optimization problem defined by equation 11 is generally underdetermined, i.e. there are many solutions $\epsilon(t)$ which achieve equally high fidelities. Therefore, we can add additional terms to the optimization cost function, such that the resulting solution optimizes against several other desiderata. For a set of constraints on the solution $\{g_i \geq 0\}$, where ideally $g_i(\epsilon(t)) = 0$, we can associate a Lagrange multiplier λ_i , and modify our optimization to read:

$$\text{maximize}_{\epsilon(t)} \mathcal{F}(\epsilon(t)) - \sum_i \lambda_i g_i(\epsilon(t)) \quad (20)$$

The values λ_i are chosen by trial-and-error, set to be just large enough that the violation of the constraint upon termination is within acceptable levels. For instance, since the output power of our AWG is limited, the pulse must obey $\epsilon(t) \leq \epsilon_{\text{max}}$ for all t . We can construct a penalty term of the form

$$g_{\text{amplitude}}(\epsilon(t)) = \int dt (|\epsilon(t)| - \epsilon_{\text{max}})^2 \Theta(|\epsilon(t)| - \epsilon_{\text{max}}) \quad (21)$$

$$= \sum_n (|\epsilon(n\Delta t)| - \epsilon_{\text{max}})^2 \Theta(|\epsilon(n\Delta t)| - \epsilon_{\text{max}}) \quad (22)$$

Since the transfer function of the lines between the AWG and the experimental system becomes more and more uncertain as one moves further away from resonance, it is also desirable to minimize the bandwidth of the applied pulses, we do this in two ways. First, we create a penalty term of the form

$$g_{\text{derivative}}(\epsilon(t)) = \int dt \left(\frac{\partial \epsilon(t)}{\partial t} \right)^2 \quad (23)$$

$$\rightarrow \sum_n (\epsilon((n+1)\Delta t) - \epsilon(n\Delta t))^2, \quad (24)$$

where equation 24 is the appropriate equivalent of equation 23 for a piecewise constant function. Additionally, we enforce a hard cutoff on the minimum and maximum frequencies allowed in the solution by reparametrizing the optimization problem in terms of the Fourier transform of the pulses [29]:

$$\text{maximize}_{\tilde{\epsilon}(\omega)} \mathcal{F}(\epsilon(t)) - \sum_i \lambda_i g_i(\epsilon(t)) \quad (25)$$

$$\text{such that } \tilde{\epsilon}(\omega) = 0 \text{ when } \omega < \omega_{\text{min}} \text{ or } \omega > \omega_{\text{max}}$$

Since computer memory is finite, we are forced to choose a photon number truncation N such that the operator \hat{a} becomes a $N \times N$ matrix. When we do this, we are in effect replacing our infinite-dimensional oscillator with a finite-dimensional qudit. This replacement is only valid if all of the system dynamics relevant for the desired state transfers occurs within the $\{|0\rangle, \dots, |N-1\rangle\}$ subspace. For generic applied drives this is not the case. In order to enforce this property, we modify the

optimization problem to find a solution which operates identically under several different values of N . Writing the fidelity as computed with a truncation N as \mathcal{F}_N , we have:

$$\text{maximize}_{\vec{\epsilon}(\omega)} \left(\sum_k \mathcal{F}_{N+k}(\epsilon(t)) \right) - \left(\sum_i \lambda_i g_i(\epsilon(t)) \right) \quad (26)$$

To enforce that the behavior is identical in the different truncations, we add the penalty term

$$g_{\text{discrepancy}}(\epsilon(t)) = \sum_{k_1 \neq k_2} (\mathcal{F}_{N+k_1}(\epsilon(t)) - \mathcal{F}_{N+k_2}(\epsilon(t)))^2 \quad (27)$$

The choice of N determines the maximum photon number population which can be populated during the pulse, and figures in determining the minimum time necessary for the operation (faster pulses can be achieved with higher N).

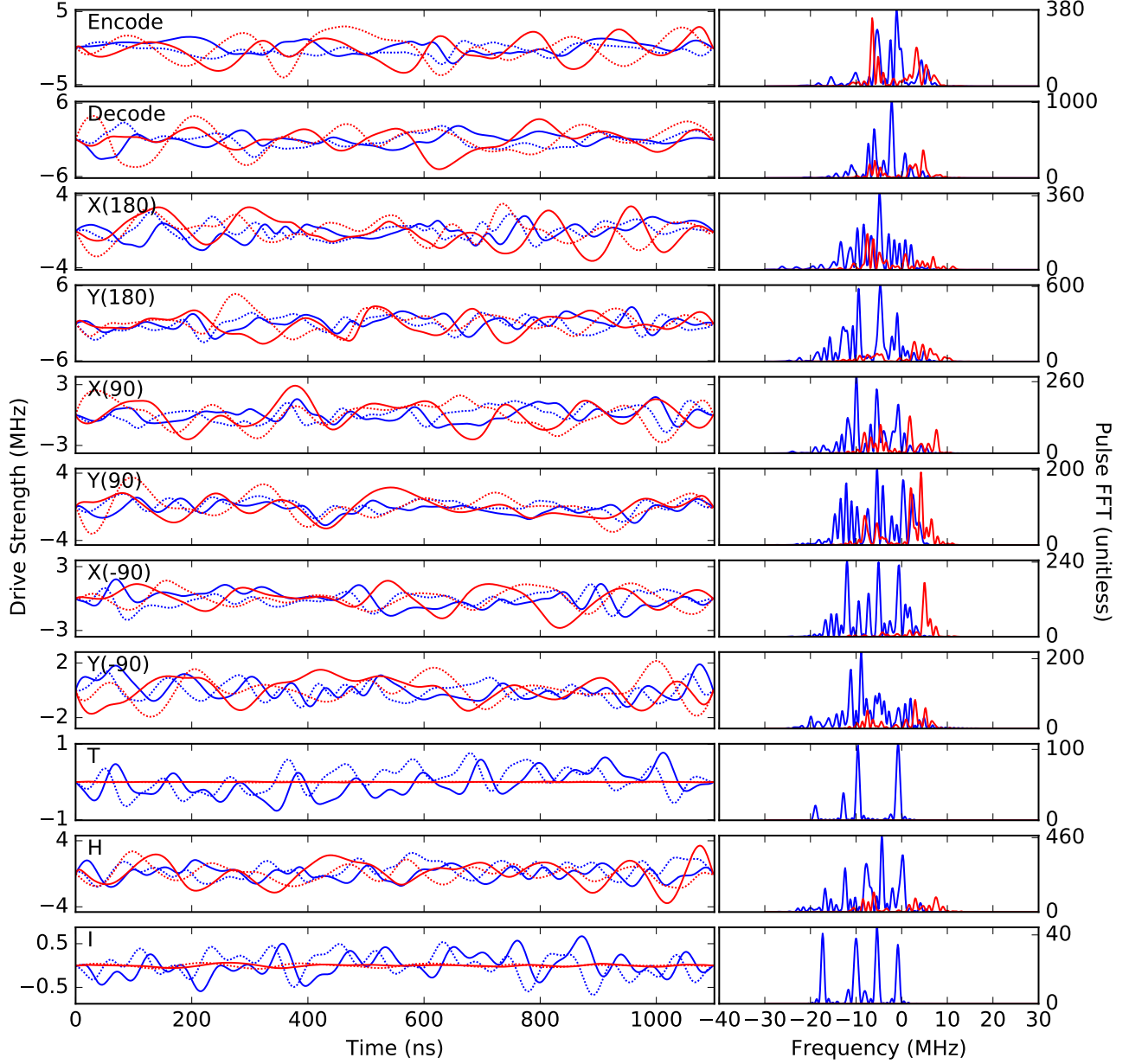


FIG. S2. **Optimized pulse waveforms.** In the first column, we plot the complex waveforms $\epsilon_T(t)$ and $\epsilon_C(t)$. In the second column, we show the Fourier spectrum $|\tilde{\epsilon}(\omega)|^2$. Blue (red) lines correspond to drives on the transmon (oscillator). Solid (dotted) lines correspond to the in-phase (quadrature) component of the drive. Note that the I and the T gate do not have to change the photon number distribution, but only have to apply different phases to each Fock state component. This can be done by manipulating the transmon [19] only; GRAPE finds a solution with a very small oscillator drive amplitude as well.

III. MEASUREMENT SETUP

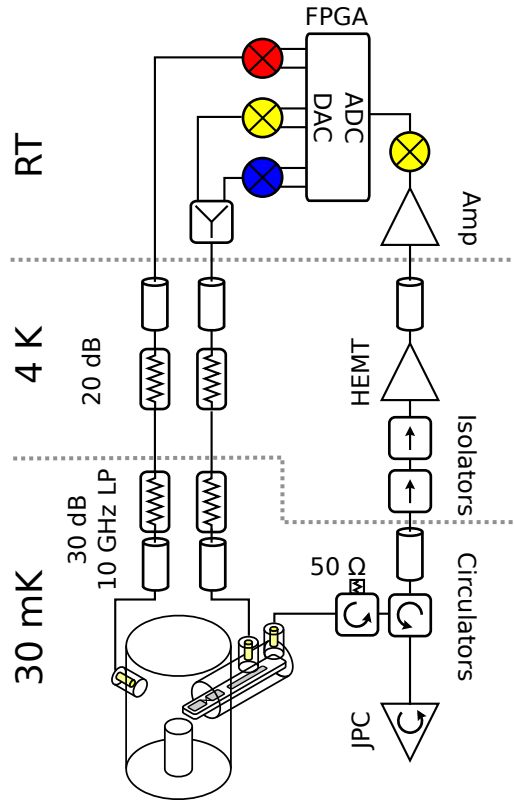


FIG. S3. **Measurement setup.** An FPGA controller (2x Innovative Integration X6-1000M in VPXI-ePC chassis) generates 3 pairs of I/Q waveforms using 500 Msample/s digital to analog converters (DAC). Each pair is upconverted using an I/Q mixer (Marki IQ-0307-LXP or IQ-0618-LXP depending on the frequency). The color of the mixer indicates the local oscillator: red for the storage, yellow for the readout and blue for the transmon. To prevent problems due to mixer leakage, each local oscillator is set 50 MHz above the desired frequency and single-sideband modulation is used. Proper attenuation at each temperature stage is crucial to thermalize the black-body radiation from the 50 Ω environment. Additional low-pass filters (K&L250-10000 and home-built eccosorb) protect the sample from spurious high-frequency components. The output chain consists of a Josephson Parametric Converter (JPC), which reflects the input signal with ~ 20 dB of gain (bandwidth ~ 6 MHz). The circulators (Pamtech XTE0812KC) prevent the amplified signal from going back to the sample and direct it through 2 isolators (Pamtech CWJ0312KI) to a HEMT-amplifier (Low Noise Factory LNF-LNR1_12A). Finally, an image reject mixer (Marki SSB-0618) converts the RF signal back to the intermediate frequency (50 MHz). The FPGA samples the signal using a 1 Gsample/s analog to digital converter (ADC), demodulates and integrates to give one bit of information indicating whether the transmon was in $|g\rangle$ or $|e\rangle$.

IV. SYSTEM PREPARATION

The system is initialized by cooling of both the storage resonator (typical steady-state population $\sim 2\%$) and the transmon (steady-state population $\sim 5\%$) using measurement-based feedback. The protocol is detailed in figure S4. It proceeds by first establishing that the oscillator is in its ground state, and finishes by ensuring that the transmon is in its ground state (figure S4a). If it is determined that the oscillator is not empty, a set of "Q-Switching" drives is applied which effectively couples the storage mode to the short-lived readout mode (figure S4b). The drives consist of strong tones applied at $\omega_C + \Delta$ and $\omega_{RO} + \Delta$ with $\Delta = 40$ MHz. The effectiveness of this strategy can be seen from the transmon spectroscopy traces (figure S4c). The transmon population is reduced to $\sim 1\%$ and the storage resonator population is $\ll 1\%$. A residual population of the readout resonator of

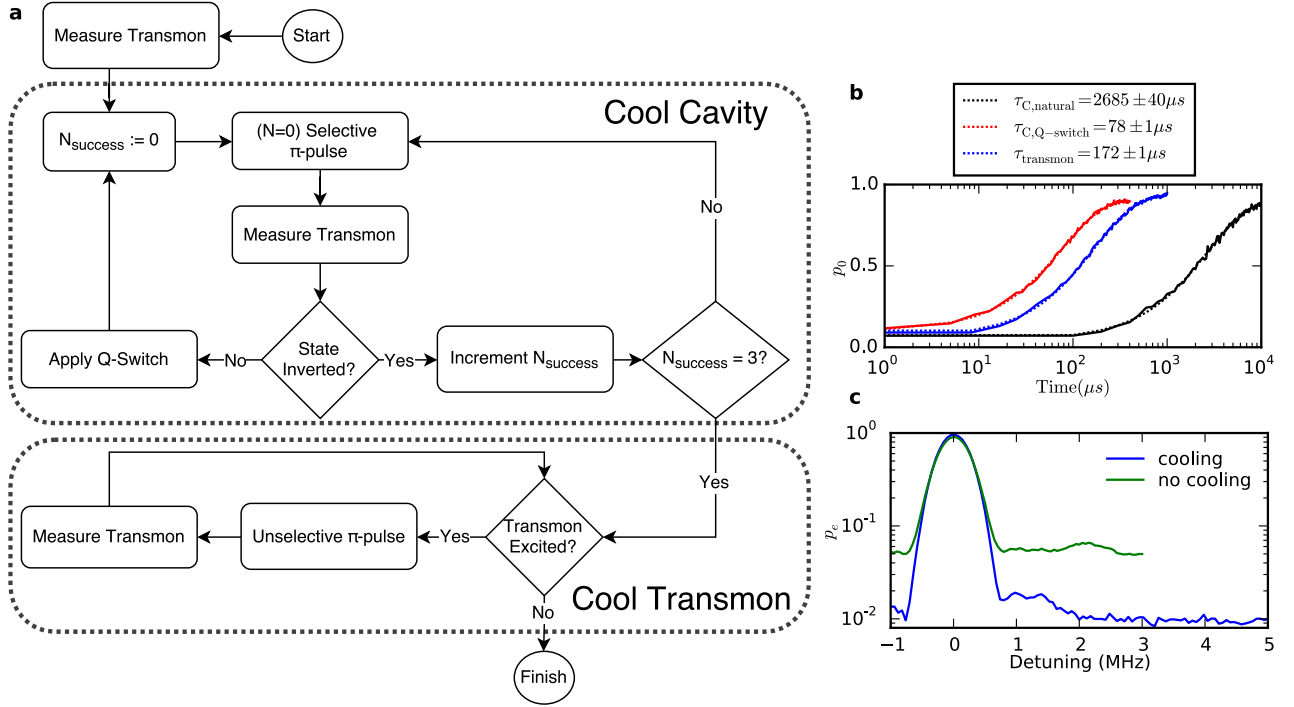


FIG. S4. **System preparation.** **a**, System preparation protocol to cool the oscillator as well as the transmon. **b**, Lifetime of the transmon and oscillator. For the oscillator we prepare the Fock state $|1\rangle$ using an optimal control pulse and show a natural decay curve as well as one with Q-switching pumps applied. **c**, Transmon spectroscopy data after system preparation. The "cooling" ("no-cooling") curve are with (without) the feedback-cooling protocol. Photons in the storage (readout) oscillator show up as a peak around $\chi_s \approx 2$ MHz ($\chi_r \approx 1$ MHz).

about 1% is visible as a peak around 1 MHz detuning. Additionally, this cooling protocol allows for a dramatically increased experimental repetition rate, decreasing the inter-experimental delay τ from $\tau \approx 18$ ms to $\tau < 1$ ms.

V. EMPIRICAL TUNING

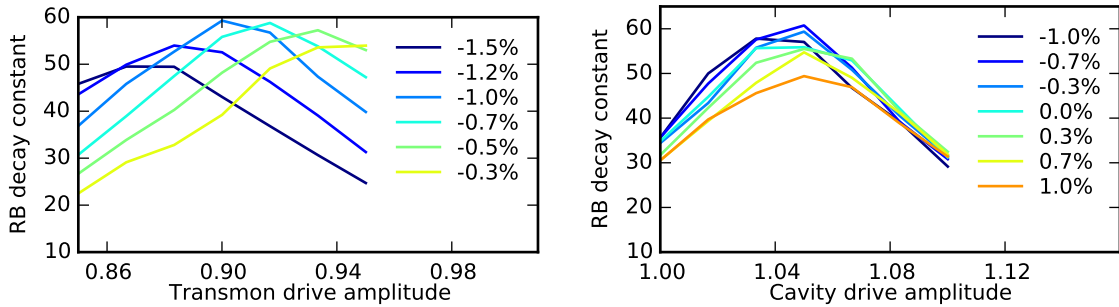


FIG. S5. **Dispersion and amplitude optimization** The randomized benchmarking decay constant versus transmon drive amplitude for several different dispersion values (in % per MHz). Because of the spectral content of the pulses, the amplitude might have to be corrected when the dispersion value is adjusted.

We use the randomized benchmarking protocol to perform fine tuning of the resulting pulse waveforms [30, 31]. Since the

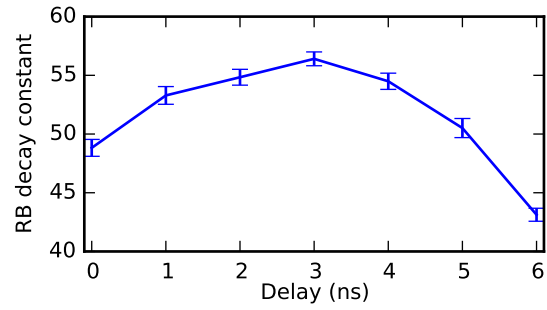


FIG. S6. Delay optimization

cables and frequency modulation setup between our waveform generator and our device are not spectrally flat, we attempt to find a correction to the pulse by applying a linear amplitude weighting in the frequency domain, i.e. Fourier transforming the waves to find $\tilde{\epsilon}(\omega)$, transforming using the weighting coefficient b and delay parameter τ . $\tilde{\epsilon}(\omega) \rightarrow (1 + b\omega e^{i\omega\tau})\tilde{\epsilon}(\omega)$, and inverse Fourier transforming to find the corrected waves in the time domain. We can empirically optimize the value of b (figure S5) and τ (figure S6) using randomized benchmarking.

VI. ADDITIONAL DATA

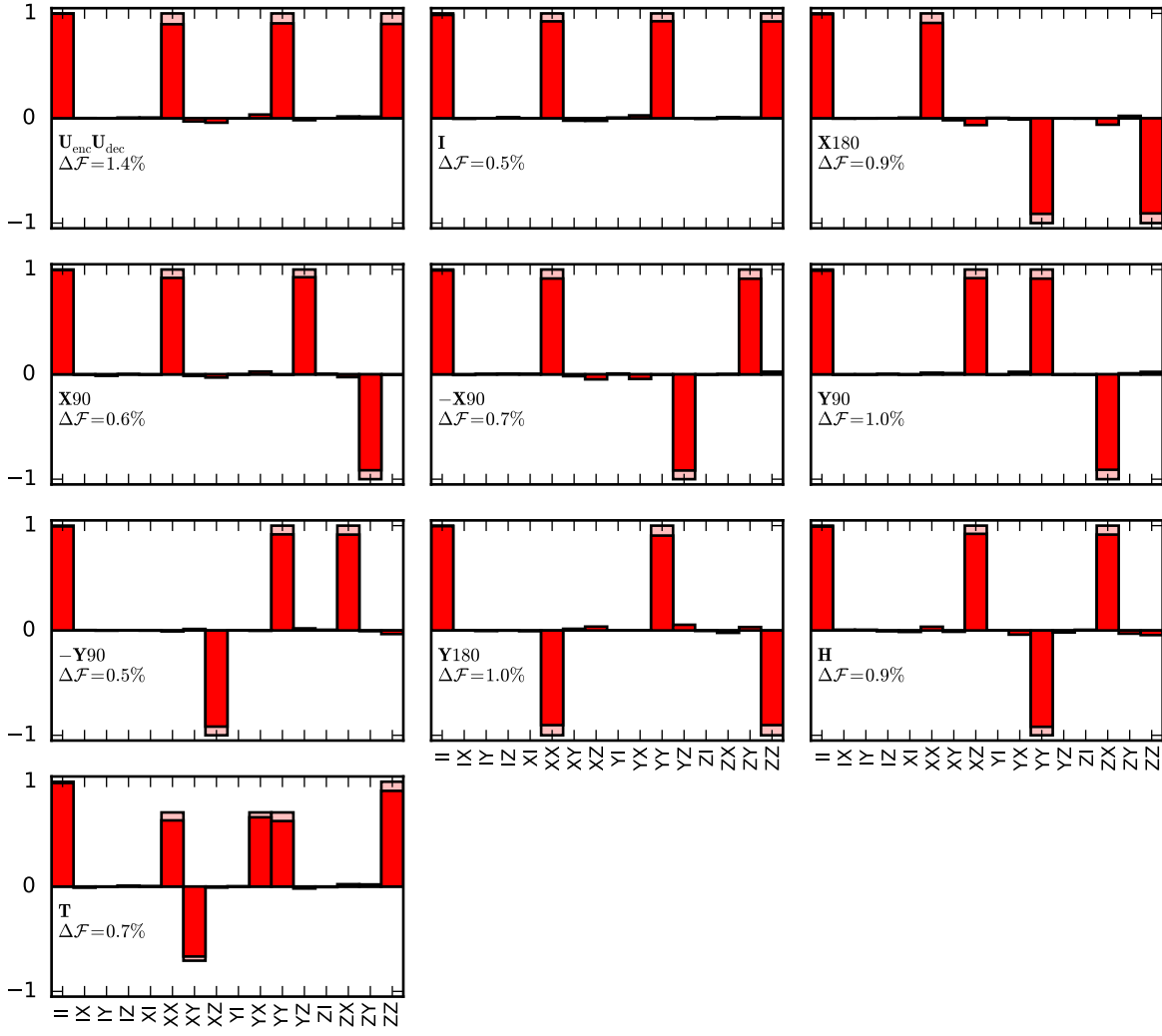


FIG. S7. Full Process Tomography Results.

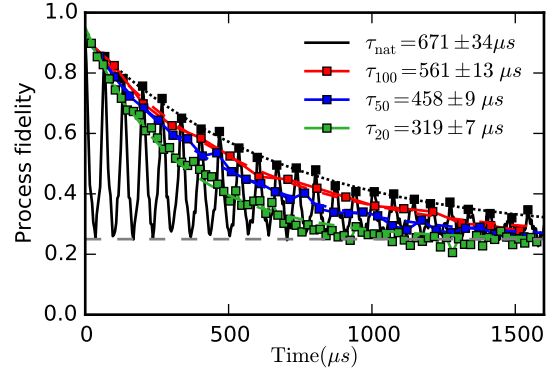


FIG. S8. **Lifetime of the cat-qubit.** The long-lived resonator is not perfectly harmonic; its Kerr is -3.7 kHz. This nonlinearity will scramble the basis-states of our encoding under free evolution. The black curve shows the process fidelity versus waiting time: periodic revivals [32] associated with rephasing of the basis-states are clearly visible. Note that the revival periodicity is not $1/K$ due to an intentional frequency detuning. Our control pulses take this effect into account during their operating time. Additionally, we can design a control pulse that corrects for the evolution associated with some time Δt of free evolution. The different curves in this plot are the result of a stroboscopic Kerr-correction experiment for 20, 50 and 100 μs of free-evolution. We can infer a Kerr-correction gate error of $\approx 1.7\%$ per gate by extracting the additional decay rate compared to the natural decay.